Optical studies of MBE-grown InN nanocolumns: Evidence of surface electron accumulation

J. Segura-Ruiz,* N. Garro, and A. Cantarero
Institut de Ciència dels Materials, Universitat de València, P.O. Box 22085, E-46071, Spain

C. Denker, J. Malindretos, and A. Rizzi
IV. Physikalisches Institut, Georg-August Universität Göttingen, Germany

(Received 23 October 2008; revised manuscript received 12 January 2009; published 6 March 2009)

Vertically self-aligned InN nanocolumns have been investigated by means of scanning electron microscopy, Raman scattering, and photoluminescence spectroscopy. Different nanocolumn morphologies corresponding to different molecular beam epitaxy growth conditions have been studied. Raman spectra revealed strain-free nanocolumns with high crystalline quality for the full set of samples studied. Longitudinal optical modes both uncoupled and coupled to an electron plasma coexist in the Raman spectra pointing to the existence of two distinctive regions in the nanocolumn: a surface layer of degenerated electrons and a nondegenerated inner core. The characteristics of the low-temperature photoluminescence and its dependence on temperature and excitation power can be explained by a model considering localized holes recombining with degenerated electrons close to the nonpolar surface. The differences observed in the optical response of different samples showing similar crystalline quality have been attributed to the variation in the electron accumulation layer with the growth conditions.

DOI: 10.1103/PhysRevB.79.115305 PACS number(s): 78.67.−n, 73.20.At, 78.30.Fs, 68.37.Hk

I. INTRODUCTION

Nanotechnology based on semiconductor nanocolumns (NCs) points out a new generation of devices benefiting from quantum confinement effects, large surface to volume ratios, and a wide design space for band-gap engineering.[1] Columnar morphology favors lateral elastic relaxation, and thus NC heterostructures and alloys admit greater lattice mismatch than thin films without the formation of defects. Group-III nitrides provide a good example of the improved crystal quality of NCs.[2] Indeed, vertically self-aligned GaN NCs grow spontaneously—no seeds or catalyst are required—with no dislocations and present intense and narrow excitonic emission peaks in the UV range.[3,4]

Recently, InN NCs have also been successfully grown by plasma-assisted molecular beam epitaxy (PAMBE) under N-rich conditions.[5–10] The interest in InN NCs relies on some of the intrinsic properties of this material, such as the 0.67 eV band-gap energy or the 0.07 m_0 electron effective mass at the Γ point.[11] The latter leads not only to high electron mobilities and high saturation velocities but also to a pronounced band-filling effect in samples with electron concentrations on the order of $10^{18}-10^{19}$ cm^{-3}.[11] Such figures are common in unintentional *n*-doped InN epilayers, for which an electron concentration (n_e) of 3×10^{17} cm^{-3} is the lowest value reported to date.[12] The first published studies revealed that there are strong differences between InN and GaN NCs. Electron-transport investigations show that the conductivity of InN NCs is several orders of magnitude higher than that of GaN NCs and proportional to the inverse of the column diameter.[13,14] On the other hand, the photoluminescence (PL) emission of InN NCs is weaker than that of thin films and presents broad and featureless peaks which are blueshifted with respect to the InN band-gap energy.[5,6,15,16]

Most of the above phenomenology has been attributed to the effects of the surface electron accumulation layer reported for InN.[17] Thermodynamic equilibrium is associated with a transfer of electrons from the surface to the bulk and with the formation of an electron accumulation layer close to the surface, as is also known for InAs.[18] This causes a downward conduction-band bending well below the Fermi level at the surface. While there is general consensus on the existence of an accumulation layer on polar (0001) surfaces, its nature at nonpolar surfaces is still under debate. On the one hand, valence-band photoemission measurements on polar and nonpolar surfaces of InN conclude that the electron accumulation layer is a universal feature of all InN surfaces.[19] However a recent theoretical study shows that nonpolar planes can behave in different manners and the presence of an electron accumulation layer depends on the surface stoichiometry.[20] Since InN NCs grow along the [0001] polar direction, their sidewalls are nonpolar planes. Thus the characteristics of the surface electron accumulation layer in these nanostructures and its dependence on the growth conditions can be analyzed.

In the present work we investigate the effects of a surface electron accumulation layer on the optical properties of InN NCs obtained under different growth conditions. In particular, we search for signatures of high electron densities in the Raman scattering spectra of the InN NC samples. This nondestructive spectroscopy is a powerful tool that provides quantitative values of not only the crystalline quality and strain fields but also free carrier concentrations of semiconductor nanostructures.[21] An electron or a hole plasma couples with the longitudinal optical phonons leading to distinctive peaks in the Raman spectra. The existence of degenerate electrons also modifies the PL mechanisms. In heavily *n*-doped semiconductors (electron concentration higher than 10^{18} cm^{-3} in the case of InN) the screening of the Coulomb interaction is responsible for the lack of excitonic and shallow donor or acceptor emission. Furthermore, the interband absorption is blueshifted with respect to the band gap of the material due to the filling of the conduction-band states, the so-called Burstein-Moss shift.[22]

TABLE I. Substrate temperature (T_s), In-BEP, N_2 flux, and rf power of the plasma source employed in the growth process of the samples studied in this work. The average height (h) and diameter (d) of the NCs and the different morphologies observed are also summarized.

Sample	T_s (°C)	In-BEP (10^{-8} mbar)	N_2 flux (sccm)	rf power (W)	h (nm)	d (nm)	Morphology
G053	400	3.0	2.0	500			layerlike
G071	475	3.0	2.0	500	500–1500	80–30	unfaceted
G047	500	3.0	2.0	500	500	180	hexagonal
G041	500	1.5	1.5	400	300	100	hexagonal
G044	500	3.0	1.5	450	360	100	hexagonal
G136	475	3.0	1.5	450	470–1500	90–40	unfaceted

This paper is organized as follows. In Sec. II, the growth of InN NCs under different conditions leading to different morphologies is briefly discussed. The optical properties of a set of samples corresponding to different growth conditions are experimentally investigated in Sec. III. First of all, the main features of the Raman scattering spectra of different InN NC morphologies are described. Then, the photoluminescence of the full set of samples studied in this work is presented. The influence of the growth parameters on the low-temperature PL is reported. Temperature and power dependences of the emission are also studied. The main experimental results of Sec. III are discussed in Sec. IV with the aid of a model that takes into account the effects of an electron accumulation layer at the NC lateral surfaces. Finally, Sec. V summarizes the main conclusions of this work.

II. DESCRIPTION OF THE NANOCOLUMN ENSEMBLE

InN NCs were grown on p-Si(111) substrates in a Veeco Gen-II MBE system. The active nitrogen was provided by an rf-plasma source (Unibulb), and N_2-rich conditions were kept in order to obtain nanocolumnar morphologies. A standard effusion cell was used as an In source. The p-Si(111) substrates were cleaned with acetone and isopropanol in an ultrasonic bath for 2 min before mounting. Afterwards the substrate was outgassed *in situ* at 600 °C for 10 h and at 1000 °C for 40 min. The resulting 7×7 reconstruction of the surface was monitored by reflection high-energy electron diffraction (RHEED) and was used as an indication of an oxygen-free Si surface. In order to limit the nitridation of the substrate, the plasma was turned on no longer than 5 min before the growth. The growth started when both In and N shutters were opened simultaneously and lasted 300 min for all samples. The substrate temperature, indium beam equivalent pressure (In-BEP), and N_2 flux used during the growth of each studied sample are summarized in Table I. Although N_2 rich conditions were kept in order to obtain columnar morphologies, the values used for all samples are considerably lower than those reported by other authors.[5–7]

The morphology of the grown NCs has been characterized by scanning electron microscopy (SEM). Figure 1 shows SEM images of four different samples grown using different parameters. Remarkable differences are observed in the morphology of samples G053, G071, and G047, evidencing the decisive role of T_s. At the upper left corner of Fig. 1, sample G053 exhibits a high density of coalescent NCs of uniform height (~250 nm). Samples grown at an intermediate temperature, such as G071, show well-separated unfaceted NCs with a bimodal aspect ratio (h/d) distribution: longer and thinner NCs have diameters and heights of ~30 nm and ~1.5 μm, respectively. Shorter NCs taper at the top. Sample G047 (lower right corner) grown at T_s=500 °C contains a lower density of NCs with a diameter almost twice as large as those previously described. These NCs exhibit clear hexagonal facets and their diameter widens toward the top end, presenting the so-called baseball bat shape.[6,15] By lowering the In-BEP, regular diameters from the bottom to the top are obtained, as observed for sample G041.

The results just described reveal that the size, shape, and density of InN NCs are mainly determined by the In adatoms diffusion. Some authors point out that at the initial stages of the growth process, In droplets should form[5,10] to enhance nucleation at specific points, giving origin to columnar growth. Since the diffusion of In increases with temperature, the density of NCs decreases for higher T_s. The bimodal growth observed at T_s=475 °C is caused by the coalescence of several small NC nuclei.[9] Other NCs however keep the original diameter and grow vertically faster than the first ones. Diffusion of the In adatoms along the sidewalls of the NC feeds the vertical growth. At T_s=475 °C, In diffusion

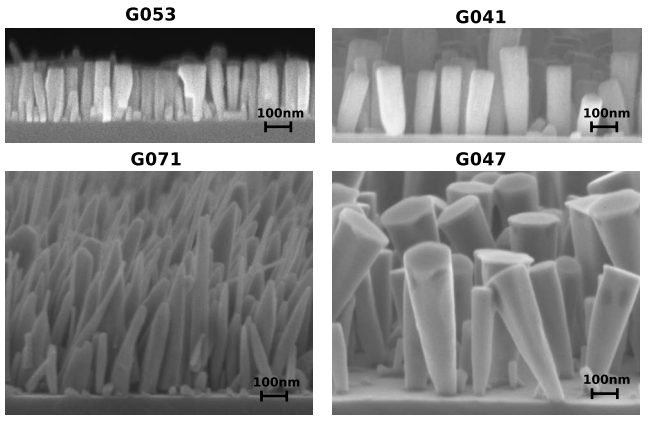

FIG. 1. SEM images of samples G053, G071, G047, and G041 illustrating the different morphologies obtained at a constant growth time of 300 min.

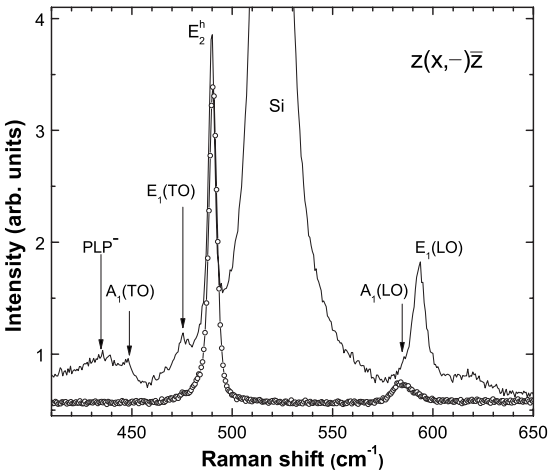

FIG. 2. Micro-Raman spectra of a representative sample of InN NCs (upper spectrum) and a high quality InN epilayer (lower spectrum) recorded at room temperature in backscattering configuration. Peaks have been labeled with their corresponding phonon modes according to the reported frequency positions for this material.

length is shorter and the NCs present tapering of their diameter toward the top. Increasing T_s slightly, T_s=500 °C, the diffusion of In atoms increases and the growth at the NC upper part is favored. Then an enlargement of the diameter toward the top is observed, showing a baseball bat shape. The variation in other growth parameters, such as the In-BEP and the N_2 flux, also affects the growth dynamics. A reduction in the In-BEP at a fixed T_s of 500 °C, for instance, causes compensation between the In adatoms' diffusion and the consumption of them at the NC top. At this quasiequilibrium condition, well-spaced, longer NCs with constant diameter could be obtained by an increase in growth time.

III. OPTICAL PROPERTIES

A. Raman scattering

Micro-Raman scattering measurements have been carried out at room temperature in backscattering configuration. The 514.5 nm line from an Ar^+ laser acted as excitation and was focused onto the sample with a 100× microscope objective with a numerical aperture of 0.90. The scattered light was dispersed by a Jobin Yvon T64000 triple spectrometer and detected with a liquid-nitrogen-cooled charge coupled device.

A representative Raman spectrum of one of the NC samples studied in this work is shown in Fig. 2 (upper spectrum). Five peaks can be observed in the studied frequency range. They have been associated with different Raman active phonons according to the reported frequency positions for InN.[23] The peaks at 489 and 588 cm^{-1} identified as the E_2^h and A_1(LO) modes, respectively, are allowed for the current scattering geometry, whereas the peaks at 447, 476, and 593 cm^{-1} coincide with the central frequencies of the A_1(TO), E_1(TO) and E_1(LO) phonons, which should be forbidden. An additional and much broader feature is also observed around 435 cm^{-1}, which does not match the frequency of any of the InN normal modes. The lower spectrum in Fig. 2 belongs to a high crystalline quality epilayer of InN. In this, only the allowed E_2^h and A_1(LO) modes are observed.

TABLE II. Frequency and FWHM of the nonpolar E_2^h mode for the full set of samples studied.

Sample	Frequency (cm^{-1})	FWHM (cm^{-1})
G053	489.3 ± 0.1	4.2 ± 0.2
G071	489.2 ± 0.1	3.5 ± 0.3
G047	489.2 ± 0.1	3.5 ± 0.3
G041	489.4 ± 0.1	3.6 ± 0.2
G044	488.9 ± 0.2	4.5 ± 0.4
G136	489.8 ± 0.1	3.0 ± 0.2

In the first place, it should be pointed out that the frequency of the nonpolar E_2^h phonons remains almost constant for all the NC samples (see Table II) and coincides with the value reported by Davydov *et al.*[23] Thus, the InN NCs are free of strain (according to the phonon deformation potentials of InN,[24] strain components are smaller than 0.1%). The second noticeable characteristic of the E_2^h peaks is their small full width at half maximum (FWHM), which evidences the high crystalline quality of the InN NCs. As a matter of fact, the FWHMs measured and summarized in Table II are among the smallest reported for InN.

The high crystalline quality of all the studied samples assures that the wave vector is conserved in the scattering process. Therefore, the appearance of forbidden peaks in the spectra cannot be associated with disorder-induced scattering. It is also unlikely that they arise from the slight lean observed in the NCs. Instead, the strength of the forbidden peaks and, in particular, the well-observed E_1(LO) mode has been explained as a consequence of the NC morphology which allows that most of the lasers light enters through and scatters from the lateral side of the NC.[25] The fact that the E_1(LO) peak, which is only allowed for right angle scattering geometry, is much more intense than the A_1(LO) should be due to the low rate top/sidewall surfaces. The absence of the forbidden modes in the spectrum of the film reinforces this assumption.

Finally, the assignment of the wide feature centered at 435 cm^{-1} is still under debate. Some authors attributed it to the low branch of the coupled plasmon-LO-phonon mode[23,25,26] (PLP$^-$), whereas a recent study points out that the PLP$^-$ could be closer to the frequency of the A_1(LO) at 586 cm^{-1} if the wave vector is not conserved.[27] Since nonconserving scattering events are disregarded in the present samples and the accumulation of free electrons at InN surfaces is a well-established fact, the PLP$^-$ seems the most suitable origin of this peak. However, the existence of coupled modes should be accompanied by the damping of the LO modes, which is not observed in the current samples. On the contrary, PLP$^-$ coexist with the LO modes in all the investigated samples, as shown in Fig. 3. This apparent contradiction is yet another signature of the presence of a high density of free electrons only at the surface while the inner part of the NC, also contributing to the Raman signal, re-

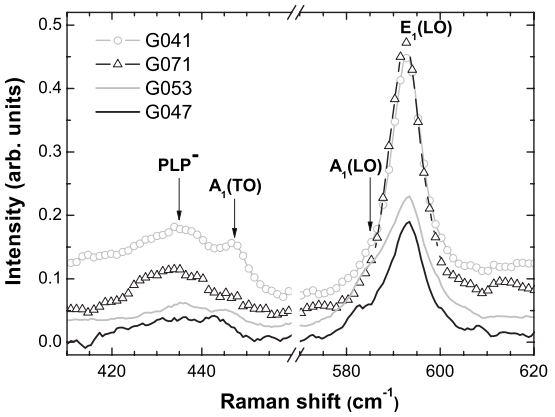

FIG. 3. Raman spectra of four representative samples showing the $A_1(\mathrm{LO})$, the $E_1(\mathrm{LO})$, and the PLP$^-$ modes. All spectra are normalized to the intensity of E_2^h, which is proportional to the total volume of excited InN.

mains almost intrinsic. Furthermore, the fact that the PLP$^-$ arises from regions closer to the NC surface, where within the first 5 nm of depth the electron density varies more than 1 order of magnitude,[17,28] also explains the large spectral broadening of this peak.

The closer analysis of the relative intensities of the PLP$^-$ and the LO modes of the different samples displayed in Fig. 3 reveals a proportionality between the intensities of the $E_1(\mathrm{LO})$ and the PLP$^-$ Raman peaks. At the same time, samples with weaker $E_1(\mathrm{LO})$ and PLP$^-$ peaks exhibit a more visible $A_1(\mathrm{LO})$ mode. As explained earlier, the $A_1(\mathrm{LO})$ to $E_1(\mathrm{LO})$ intensity ratio should be proportional to the ratio top/sidewall of the NCs. This is verified from the comparison of Figs. 1 and 3, where those samples with NC morphologies benefiting the scattering through the lateral walls present an enhanced $E_1(\mathrm{LO})$ intensity and an almost absent $A_1(\mathrm{LO})$. Thus, the Raman spectra of NCs presenting tapering effect (sample G071) or constant diameter (G041) exhibit more intense $E_1(\mathrm{LO})$ peaks than those with baseball bat shape (G047) or coalescent NCs (G053). The same behavior is observed for the PLP$^-$ mode, indicating that most of the PLP$^-$ signal arises from the sidewalls of NCs. This result is experimental evidence of free electron accumulation at the nonpolar surfaces of InN.

B. Photoluminescence

Photoluminescence measurements were performed in a close-cycle He cryostat kept at a controlled temperature. The excitation source was the 647 nm line from an Ar^+/Kr^+ laser and the PL signal was dispersed in a 0.19 m monochromator with a 600 groove/mm grating and detected with a liquid-nitrogen-cooled InGaAs photodiode.

Figure 4 shows the PL spectra of a high quality InN epilayer and the InN NCs of sample G041, taken under identical experimental conditions. The energy and spectral linewidth of the NCs emission are slightly blueshifted (~30 meV) and broadened when compared to that of the thin film. However, contrary to previous investigations,[6] both spectra show comparable intensities which denote that the

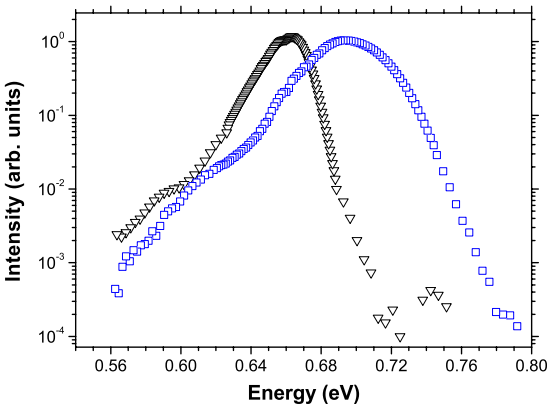

FIG. 4. (Color online) Photoluminescence spectra taken at 7 K under the same excitation conditions for NCs of sample G041 (squares) and a high quality InN epilayer (triangles).

NCs have similar radiative emission efficiency. The NCs spectrum exhibits a structure with at least two different contributions, similar to that previously observed in high quality InN films and ascribed to the radiative recombination of holes trapped at different acceptor states.[29,30] Such features were only observed in the emission of NCs of sample G041, whereas other NCs presented a single peak.

There is a strong influence of the growth conditions on the PL spectra of InN NCs, as can be seen in Fig. 5. As a matter of fact, all the PL characteristics—peak energy, broadening, and intensity—differ substantially among the studied set. The spectra of Fig. 5 correspond to three samples grown at the same T_s, presenting similar NC morphology and showing similar crystalline quality as studied by Raman scattering. Differences on the order of 50 meV are observed in the emission energy, while the emission intensity varies almost by 1 order of magnitude. It should be also noticed that the NC emission peak is asymmetric, showing a longer tail at the

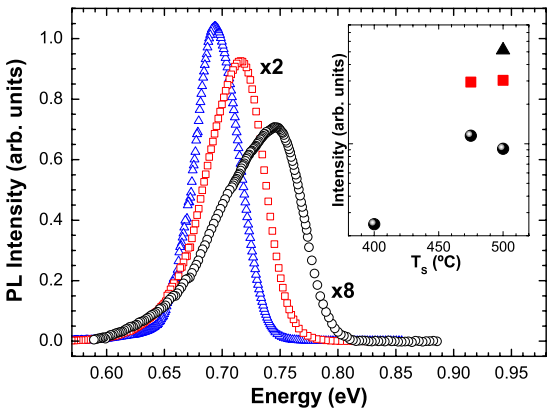

FIG. 5. (Color online) PL spectra of three samples—G041 (triangles), G044 (squares), and G047 (circles)—grown at $T_s = 500\ ^\circ\mathrm{C}$ using different In-BEP and N_2 flux conditions (see Table I). Spectra of samples G044 and G047 are scaled by a factor of 2 and 8, respectively. Inset: PL integrated intensity as a function of T_s for samples grown with an In-BEP of 3×10^{-8} mbar and two different N_2 fluxes: 2 sccm (full circles) and 1.5 sccm (full squares). The sample grown with the lowest N_2 flux and a lower In-BEP of 1.5×10^{-8} mbar is also shown (full triangles).

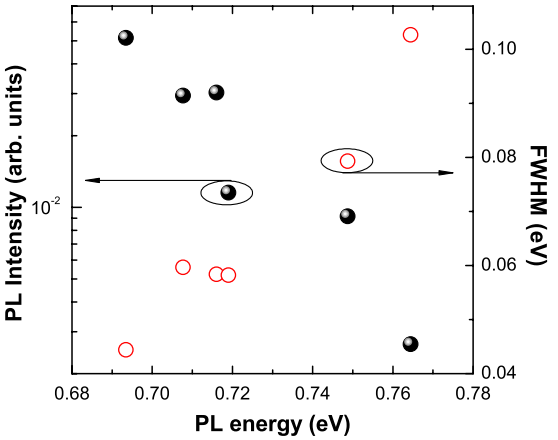

FIG. 6. (Color online) Integrated intensity (full circles) and FWHM (circles) of the PL spectra taken at 7 K for the full set of samples studied, plotted as a function of the peak energy.

low energy side. The reported asymmetry increases with the energy of the PL peak.

The integrated intensity of the PL peak plotted as a function of T_s is shown in the inset of Fig. 5 for the full set of samples studied. NCs grown with identical In-BEP and N_2 flux are represented by the same symbol. Two main conclusions can be extracted from this figure: in the first place, for identical In and N_2 fluxes, the optimal T_s is 475 °C; second, lower growth rates, achieved by lowering the In and N_2 fluxes, improve the PL intensity. The former conclusion disagrees with previous results, where the PL intensity is continuously increased with T_s from 440 up to 525 °C.[5]

We have observed a correlation between integrated intensity, line width, and energy position of the PL peak. Figure 6 shows the integrated intensity and FWHM of the PL peaks as a function of their central energy. It is observed that narrower peaks with higher intensities are also centered at lower energy. The presence of an electron accumulation layer at the NC surfaces could explain such dependence, as will be discussed in Sec. IV.

In order to shed more light on the nature of the PL in InN NCs, temperature-dependent PL experiments have been carried out from 7 to 300 K. Figure 7(a) shows the PL peak energy as a function of temperature for two representative samples. Neither of them exhibits a clear redshift with increasing temperature as compared to the 50–60 meV shift measured for bulk InN band gap from 4 to 300 K.[30,31] The PL spectra broaden with temperature for all samples. This behavior is however stronger for peaks with smaller FWHM at low temperatures, as can be observed in Fig. 7(b).

The PL integrated intensity decreases rapidly with increasing temperature, as shown for a representative sample in the Arrhenius plot of Fig. 8. The intensity decay can be well fitted, considering two different quenching mechanisms for the PL with activation energies E_1 and E_2;[32]

$$I(T) = \frac{I_0}{1 + A\,\exp(-E_1/kT) + B\,\exp(-E_2/kT)}. \qquad (1)$$

If the radiative lifetime is assumed to be temperature independent, A and B are proportional to the scattering rate of

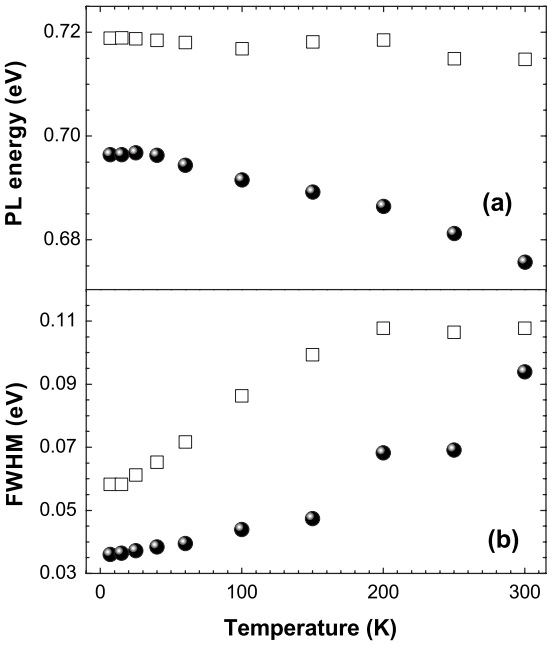

FIG. 7. (a) Energy and (b) FWHM of the PL peak as a function of the temperature for two representative samples: G041 (full circles) and G071 (squares). The PL was excited with a high power of 34.4 W/cm^2 in order to obtain measurable signals at room temperature.

each mechanism. The inset of Fig. 8 shows the fitting parameters for the full set of samples. Values of the activation energies are in good agreement with those reported for shallow and deep acceptor states in high quality InN layers.[29,30] This suggests that quenching could be due to the thermal delocalization of holes from acceptor levels, followed by nonradiative recombination. The values of parameters A and B obtained from the fitting point out that the PL quenching in our samples is mainly due to the delocalization of holes from deep acceptors. A third quenching mechanism can be added to Eq. (1) in order to improve the fitting at high temperature. The activation energy obtained for this mechanism is

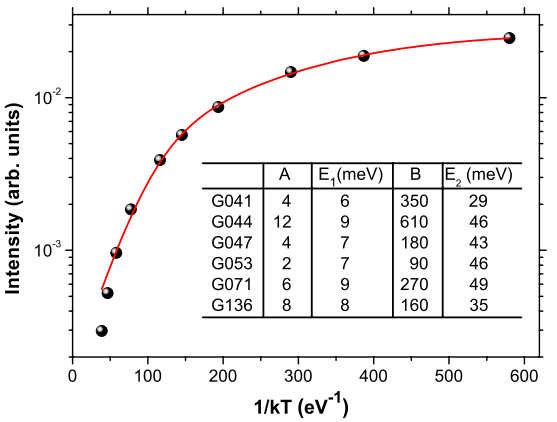

	A	E_1(meV)	B	E_2 (meV)
G041	4	6	350	29
G044	12	9	610	46
G047	4	7	180	43
G053	2	7	90	46
G071	6	9	270	49
G136	8	8	160	35

FIG. 8. (Color online) Arrhenius plot of the integrated PL intensity for sample G136 and the fitting using Eq. (1) (solid line). Inset: values of the main parameters given in Eq. (1) obtained from the best fitting of the PL integrated intensity of each sample.

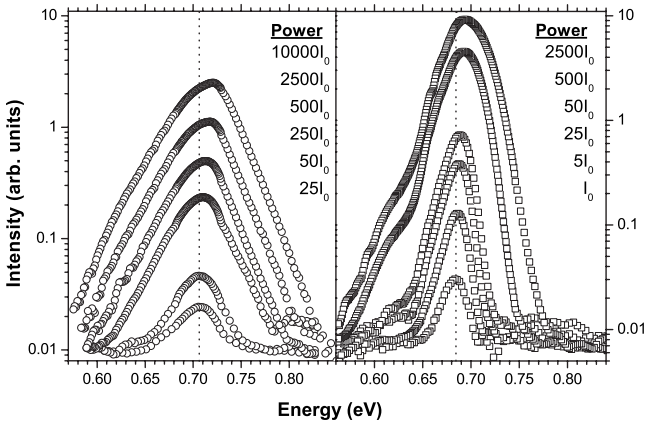

FIG. 9. PL spectra of two representative samples, G071 (left-hand side) and G041 (right-hand side), taken at 7 K and using a wide range of power excitations. I_0=0.014 W/cm^2.

160 ± 20 meV, and its physical meaning is still unclear.

Finally, PL spectra varying the excitation power density over a wide range have been also recorded. The integrated intensity of PL peak has a slightly sublinear dependence on power excitation density, $I \propto \Phi^m$, with m values ranging from 0.8 to 1. Such a sublinear dependence is attributed to the cases of free-to-bound and donor-acceptor recombinations.[33] Due to the high n_e evidenced in our samples, donor levels should not be dominant in the recombination process. Thus, the former result is another signature that acceptor levels are involved in the radiative recombination giving origin to the PL of our InN NCs. Spectra of two different samples, G041 and G071, taken under different excitation power densities ranging from 0.014 to 140 W/cm^2 are shown in Fig. 9. Sample G071 exhibits a single peak, which broadens and blueshifts with increasing excitation power but without changes in its line shape. The same features are observed for most of the samples studied in this work. This behavior has been observed for the PL spectra of highly doped InN, with electron concentrations above 10^{18} cm^{-3}.[30] Sample G041 exhibits a different behavior than the other samples studied here. At very low excitation power, a single peak centered around 685 meV is observed. As the excitation is increased, the PL peak blueshifts and broadens as in the other samples, but also a weak peak emerges at a lower energy for power excitations above 0.35 W/cm^2. The capability to observe this structure in the PL spectrum suggests a lower electron concentration in this sample,[29,30] in agreement with its lower peak energy. The two contributions to the PL band are separated around 72 meV, and no redistribution of the intensities is observed between them in the wide range of power excitation studied. This energy coincides with the LO-phonon energy obtained from our Raman measurements. All these features are in concordance with those observed for the two peaks contributing to the PL spectra of InN layers, with electron concentrations around 10^{18} cm^{-3}.[30] These peaks were ascribed to the radiative recombination of holes trapped at deep acceptor levels and its LO-phonon replica.

The high electron concentration evidenced in our samples implies that the PL of the InN NCs comes from the recombination of degenerated electrons with holes trapped at deep acceptor levels. Contributions from excitons and holes at shallow acceptors should be disregarded due to the screening of the Coulomb interaction.

IV. DISCUSSION

The Raman scattering and PL results described in Sec. III show that the optical response of InN NCs deviates from that of the bulk materials. Most of the effects just reported—such as the coexistence of plasma coupled and uncoupled LO modes in the Raman spectra; the blueshift of the PL peak with respect to the bulk InN band gap, the correlation between energy, intensity, and FWHM of the PL peaks; and the reduction in PL energy redshift with temperature—can be interpreted as signatures of a region with high density of free electrons close to the NC surfaces.

There are plenty of experimental evidences of the existence of an electron accumulation layer on polar and nonpolar surfaces of InN films.[14,17] Nevertheless, its physical origin is not yet clear, and while some studies suggest that it is an intrinsic effect due to the surface states energies,[20] others predict thickness-dependent doping mechanisms such as nitrogen vacancies associated with threading dislocations.[34,35] Keeping its nature aside, there is an excess of positive charges at the polar and nonpolar surfaces of InN that induces the bending of the conduction and the valence bands and an inhomogeneous distribution of free electrons in the crystal. Charge and band-bending profiles are usually calculated by solving Poisson's equation numerically within the modified Thomas-Fermi approximation.[36,37] In a recent article, Klochikhin *et al.*[38] presented the analytical solution of the classical Thomas-Fermi equation for a planar accumulation layer in the parabolic band approximation. Their expression for the electrostatic Coulomb potential as a function of the depth, z, is

$$-e\phi(z) = R_H \alpha \left(\frac{a_B}{z+l} \right)^4, \tag{2}$$

where R_H and a_B are the Rydberg and Bohr radius of the hydrogen atom, respectively. The parameters α and l, defined as

$$\alpha = \left(\frac{30\pi\varepsilon}{2} \right)^2 \left(\frac{m_0}{m^*} \right)^3 \tag{3}$$

and

$$l = \left(\frac{2\alpha a_B^3}{N_{SS}} \right)^{1/5}, \tag{4}$$

depend on the material properties: the electron effective mass m^*, the dielectric constant ε, and the surface density of positive charge N_{SS}. The electron distribution in the crystal is then given by

$$n_e(z) = \frac{1}{3\pi^2} \left(\frac{2m^*}{\hbar^2} \right)^{3/2} [E_F - e\phi(z)]^{3/2}, \tag{5}$$

where E_F is the Fermi level energy. Although these expressions are valid for a planar surface, they can be taken as a

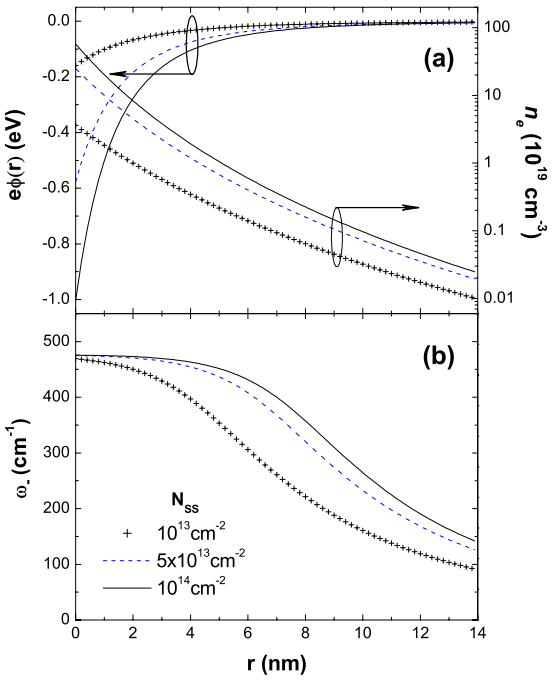

FIG. 10. (Color online) (a) Calculated depth profile of downward bending of the conduction-band minimum (left axis) and the corresponding electron distribution (right axis). Different surface charge densities ranging from 10^{13} to 10^{14} cm^{-2} have been considered. (b) Depth profile of the frequency of the PLP$^-$ mode.

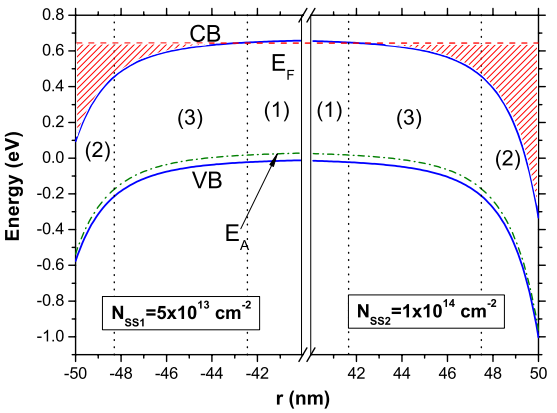

FIG. 11. (Color online) Calculated depth profile of downward bending of the CBM and the VBM for two different NCs with N_{SS} of 5×10^{13} cm^{-2} (left-hand side) and 10^{14} cm^{-2} (right-hand side). The three different regions with different probability for radiative recombination are indicated.

good first approximation for the cylindrical and hexagonal NCs investigated in this work, taking into account that most of them have a large diameter compared with the Debye length. The shape of the potential and the electron distribution are shown in Fig. 10(a) as a function of the radial coordinate r (r=0 at the surface). An effective mass of $m^*=0.25m_0$ was assumed to account for the nonparabolicity of the conduction band.[38] The Fermi level energy has been assumed to be 10 meV below the conduction band minimum in the bulk. This is a reasonable value for high quality samples. Different surface charge densities are taken within the range of values determined by other techniques.[17,39] Furthermore, recent first-principles calculations have shown that the density of positive charge at the nonpolar surfaces of InN depends on the surface stoichiometry and could, therefore, vary with the growth conditions.[20]

The inhomogeneous electron distribution depicted in Fig. 10(a) confirms the existence of two distinct regions in an InN NC: a thin layer close to the surface where n_e reaches values of the order of 10^{20} cm^{-3} and decreases by more than 2 orders of magnitude over 6–10 nm; the inner core of the NC where, in the absence of substantial unintentional doping as expected for the high crystalline quality NCs studied here, the semiconductor should have a very low n_e. This is in good agreement with the coexistence of coupled and uncoupled phonon modes observed in the Raman spectra of InN NCs (see Fig. 3). On the other hand, the rapid variation in n_e induces the depth profile of the frequency of the PLP$^-$ mode shown in Fig. 10(b). The coupled mode frequencies depend on the LO phonon (ω_L), the TO phonon (ω_T), and the plasma (ω_p) frequencies as[40]

$$\omega_{\pm}^2 = \frac{\omega_L^2+\omega_p^2}{2} \pm \frac{\sqrt{(\omega_L^2+\omega_p^2)-4\omega_p^2\omega_T^2}}{2}. \quad (6)$$

The dispersion of ω_- shown in Fig. 10(b) is in agreement with the large broadening and the low frequency tail observed for the PLP$^-$ feature of the NC Raman spectra. On the other hand, the central frequency measured for the PLP$^-$ mode ($\sim$435 cm^{-1}) tells us that the electron concentration reaches values on the order of 10^{19} cm^{-3} close to the NC surfaces.

The conduction- and valence-band bending and the large concentration of degenerated electrons just reported should have a strong effect on the NCs emission. In order to clarify the process leading to PL formation, the profiles of the valence-band maximum (VBM) and the conduction-band minimum (CBM) are plotted as a function of the NC radius in Fig. 11 for two different values of N_{SS}. The same Fermi level is assumed for both situations since its value depends mostly on the electron concentration away from the surface for nanocolumn diameters above 50 nm.[41] In the PL process, the photogenerated electrons and holes are driven in opposite directions by the electric field induced by N_{SS}. Thus, while electrons accumulate at the surfaces, holes should be located in the inner core of the NCs. The probability of radiative recombination is proportional to the spatial overlap of the electron and hole wave functions. Therefore, according to the probability of radiative recombination, three different regions can be identified inside the NCs: (1) the NC core with a marginal radiative recombination probability due to the absence of photogenerated electrons, which shall move fast to the NC surfaces; (2) the most external region, close to the NC surface where the lack of holes, drifted toward the center by the electric field also reduces the radiative recombination rate; and finally (3) an intermediate region populated by both electrons and photogenerated holes, most probably trapped at impurities thanks to the weakness of the electric field. The last region is the most active from the optical point of view.

The scheme presented in Fig. 11 can help us understand most of the properties reported for the InN NCs PL. First, the

blueshift of the NCs emission with respect to bulk InN band gap is a manifestation of the Burstein-Moss shift that takes place at the optically active regions of the NCs. The existence of bound holes at acceptor levels evidenced in Sec. III allows for the breakdown of the momentum conservation selection rule and all the electrons in the conduction band can contribute to the emission. Then, the maximum of the PL emission should appear at an energy between the conduction-band minimum and the absorption edge, giving origin to the observed blueshift. On the other hand, the relationship among energy, FWHM, and intensity of the PL peaks displayed in Fig. 6 can be explained considering that different NCs have different N_{SS}. As shown in Fig. 11, NCs with higher N_{SS} should have smaller optically active volumes which should lead to lower PL intensities. At the same time the higher n_e of these NCs results in higher emission energies and larger broadenings. Finally, when increasing the sample's temperature, photoholes can spread over a wider region penetrating deeper into the electron accumulation layer. This should induce a blueshift and an additional broadening of the PL peak, which compensates the normal redshift due to the temperature dependence of the band gap. InN NCs with higher N_{SS} at the surface shall therefore show a larger reduction in the thermal redshift and a faster increase in the FWHM of their PL peaks. This is in very good agreement with the experimental findings of Fig. 8.

Finally, we turn our attention to the asymmetric line shape of the PL peak observed in Fig. 5. The same trend has been reported in recent studies and attributed to the recombination of degenerated electrons and localized holes.[42] Hole localization relaxes the wave-vector conservation in the radiative recombination process. Thus the PL line shape reveals the electron density of states: a low energy tail due from the bottom of the conduction band and a sharper high energy edge due to the cutoff of the Fermi occupation function.

V. CONCLUSIONS

In this paper we have presented SEM, Raman, and PL measurements of MBE-grown InN NCs. The variation in growth conditions has led to different NC morphologies, which exhibited no strain and high crystalline quality. The coexistence of a coupled PLP and LO modes and the analysis of their relative intensities for different NC morphologies gave evidence of the electron accumulation at the nonpolar lateral surfaces of the NCs while their inner cores remained intrinsic. Clear differences were observed in the energy, peak width, and intensity of the PL spectra of InN NCs grown under different conditions, even among those with identical morphologies. Temperature and power dependences of the PL peak pointed out that localized holes are involved in the radiative recombination. A model for the PL formation, where localized holes recombine with degenerated electrons in a NC region close to the surface, explained well the characteristics of the PL at low temperature and its dependence on temperature and power excitation. The differences observed in the PL spectra of samples grown under different conditions were explained by variations in the density of positive charge at the nonpolar NC surfaces.

ACKNOWLEDGMENTS

We acknowledge D. Mai for helpful assistance in the MBE growth. This work was supported by the ER-ANET project "NanoSci-ERA: NanoScience in the European Research Area" of the EU FP6 and by ministry of science and education (Grant No. MAT2006-01825). J.S.-R. thanks the Ministerio de Educación y Ciencia of Spain for financial support through a FPU grant.

*jaime.segura@uv.es

[1] T. Kuykendall, P. Ulrich, S. Aloni, and P. Yang, Nature Mater. **6**, 951 (2007).

[2] For a review, see E. Calleja, J. Ristić, S. Fernández-Garrido, L. Cerutti, M. A. Sánchez-García, J. Grandal, A. Trampert, U. Jahn, G. Sánchez, A. Griol, and B. Sánchez, Phys. Status Solidi B **244**, 2816 (2007)

[3] L. Cerutti, J. Ristić, S. Fernández-Garrido, E. Calleja, A. Trampert, K. H. Ploog, S. Lazic, and J. M. Calleja, Appl. Phys. Lett. **88**, 213114 (2006).

[4] R. Songmuang, O. Landré, and B. Daudin, Appl. Phys. Lett. **91**, 251902 (2007).

[5] T. Stoica, R. Meijers, R. Calarco, T. Richter, and H. Lüth, J. Cryst. Growth **290**, 241 (2006).

[6] C.-H. Shen, H.-Y. Chen, H.-W. Lin, S. Gwo, V. Yu. Davydov, and A. A. Klochikhin, Appl. Phys. Lett. **88**, 253104 (2006).

[7] M. A. Sánchez-García, J. Grandal, E. Calleja, S. Lazic, J. M. Calleja, and A. Trampert, Phys. Status Solidi B **243**, 1490 (2006)

[8] J. Grandal, M. A. Sánchez-García, E. Calleja, E. Luna, and A. Trampert, Appl. Phys. Lett. **91**, 021902 (2007).

[9] C. Denker, J. Malindretos, F. Werner, F. Limbach, H. Schuhmann, T. Niermann, M. Seibt, and Angela Rizzi, Phys. Status Solidi C **5**, 1706 (2008).

[10] S. Nishikawa, Y. Nakao, H. Naoi, T. Araki, H. Na, and Y. Nanishi, J. Cryst. Growth **301-302**, 490 (2007).

[11] W. Walukiewicz, J. W. Ager III, K. M. Yu, Z. Liliental-Weber, J. Wu, S. X. Li, R. E. Jones, and J. D. Denlinger, J. Phys. D **39**, R83 (2006).

[12] H. Lu, W. J. Schaff, J. Hwang, H. Wu, G. Koley, and L. F. Eastman, Appl. Phys. Lett. **79**, 1489 (2001).

[13] R. Calarco and M. Marso, Appl. Phys. A: Mater. Sci. Process. **A87**, 499 (2007).

[14] E. Calleja, J. Grandal, M. A. Sánchez-García, M. Niebelschütz, V. Cimalla, and O. Ambacher, Appl. Phys. Lett. **90**, 262110 (2007).

[15] H.-Y. Chen, C.-H. Shen, H.-W. Lin, C.-H. Chen, C.-Y. Wu, S. Gwo, V. Yu. Davydov, and A. A. Klochikhin, Thin Solid Films **515**, 961 (2006).

[16] T. Stoica, R. J. Meijers, R. Calarco, T. Richter, E. Sutter, and H.

Lüth, Nano Lett. **6**, 1541 (2006).
[17] I. Mahboob, T. D. Veal, C. F. McConville, H. Lu, and W. J. Schaff, Phys. Rev. Lett. **92**, 036804 (2004); I. Mahboob, T. D. Veal, L. F. J. Piper, C. F. McConville, H. Lu, W. J. Schaff, J. Furthmüller, and F. Bechstedt, Phys. Rev. B **69**, 201307(R) (2004).
[18] M. Noguchi, K. Hirakawa, and T. Ikoma, Phys. Rev. Lett. **66**, 2243 (1991).
[19] P. D. C. King, T. D. Veal, C. F. McConville, F. Fuchs, J. Furthmuller, F. Bechstedt, P. Schley, and R. Goldhahn, Appl. Phys. Lett. **91**, 092101 (2007).
[20] C. G. Van de Walle and D. Segev, J. Appl. Phys. **101**, 081704 (2007).
[21] H. Harima, J. Phys.: Condens. Matter **14**, R967 (2002).
[22] E. Burstein, Phys. Rev. **93**, 632 (1954).
[23] V. Y. Davydov, V. V. Emtsev, I. N. Goncharuk, A. N. Smirnov, V. D. Petrikov, V. V. Mamutin, V. A. Vekshin, S. V. Ivanov, M. B. Smirnov, and T. Inushima, Appl. Phys. Lett. **75**, 3297 (1999).
[24] X. Wang, S. B. Che, Y. Ishitani, and A. Yoshikawa, Appl. Phys. Lett. **89**, 171907 (2006).
[25] S. Lazic, E. Gallardo, J. M. Calleja, F. Agullo-Rueda, J. Grandal, M. A. Sanchez-Garcia, E. Calleja, E. Luna, and A. Trampert, Phys. Rev. B **76**, 205319 (2007).
[26] J. W. Chen, Y. F. Chen, H. Lu, and W. J. Schaff, Appl. Phys. Lett. **87**, 041907 (2005).
[27] J. W. Pomeroy, M. Kuball, C. H. Swartz, T. H. Myers, H. Lu, and W. J. Schaff, Phys. Rev. B **75**, 035205 (2007).
[28] A. A. Klochikhin, V. Y. Davydov, I. Y. Strashkova, and S. Gwo, Phys. Rev. B **76**, 235325 (2007).
[29] B. Arnaudov, T. Paskova, P. P. Paskov, B. Magnusson, E. Valcheva, B. Monemar, H. Lu, W. J. Schaff, H. Amano, and I. Akasaki, Phys. Rev. B **69**, 115216 (2004).
[30] A. A. Klochikhin, V. Yu. Davydov, V. V. Emtsev, A. V. Sakharov, V. A. Kapitonov, B. A. Andreev, Hai Lu, and W. J. Schaff, Phys. Rev. B **71**, 195207 (2005).
[31] J. Wu, W. Walukiewicz, W. Shan, K. M. Yu, J. W. Ager III, S. X. Li, E. E. Haller, Hai Lu, and W. J. Schaff, J. Appl. Phys. **94**, 4457 (2003).
[32] E. M. Daly, T. J. Glynn, J. D. Lambkin, L. Considine, and S. Walsh, Phys. Rev. B **52**, 4696 (1995).
[33] T. Schmidt, K. Lischka, and W. Zulehner, Phys. Rev. B **45**, 8989 (1992).
[34] V. Cimalla, V. Lebedev, C. Y. Wang, M. Ali, G. Ecke, V. M. Polyakov, F. Schwierz, O. Ambacher, H. Lu, and W. J. Schaff, Appl. Phys. Lett. **90**, 152106 (2007).
[35] L. F. J. Piper, T. D. Veal, C. F. McConville, H. Lu, and W. J. Schaff, Appl. Phys. Lett. **88**, 252109 (2006).
[36] T. D. Veal, L. F. J. Piper, W. J. Schaff, and C. F. McConville, J. Cryst. Growth **288**, 268 (2006).
[37] P. D. C. King, T. D. Veal, and C. F. McConville, Phys. Rev. B **77**, 125305 (2008).
[38] A. A. Klochikhin, V. Y. Davydov, I. Y. Strashkova, P. N. Brunkov, A. A. Gutkin, M. E. Rudinsky, H. Y. Chen, and S. Gwo, Phys. Status Solidi (RRL) **1**, 159 (2007).
[39] H. Lu, W. J. Schaff, L. F. Eastman, and C. E. Stutz, Appl. Phys. Lett. **82**, 1736 (2003).
[40] E. Burstein, A. Pinczuk, and S. Iwasa, Phys. Rev. **157**, 611 (1967).
[41] J. Segura-Ruiz, A. Molina-Sánchez, F. Iikawa, N. Garro, A. García-Cristóbal, A. Cantarero, C. Denker, J. Malindretos, and A. Rizzi (to be published).
[42] M. Feneberg, J. Däubler, K. Thonke, R. Sauer, P. Schley, and R. Goldhahn, Phys. Rev. B **77**, 245207 (2008).